BIOMIMETICS

Sticking the landing: Insect-inspired strategies for safely landing flapping-wing aerial microrobots

Nak-seung P. Hyun[1,2]†, Christian M. Chan[1]†, Alyssa M. Hernandez[1], Robert J. Wood[1]*

For flying insects, the transition from flight to surface locomotion requires effective touchdown maneuvers that allow stable landings on a variety of surfaces. Landing behaviors of insects are diverse, with some using more controlled flight approaches to landing, whereas others dampen collision impacts with parts of their bodies. The landing approaches of real insects inspired our current work, where we present a combined mechanical and control approach to achieving safe and accurate landings for flapping-wing microaerial vehicles. For the mechanical approach to landing, we took inspiration from the legs of the crane fly, designing lossy compliant legs that maximize energy dissipation during surface collisions. We explored three features in the compliant leg design: leg stance, number of joints, and joint placement. For the control approach to landing, the challenge lies in overcoming the aerodynamic ground effect near the surface. Leveraging the compliant leg design during impact, we designed the preimpact behavior, drawing inspiration from insect landing trajectories, to increase landing success. The proposed controlled landing sequence includes an initial acceleration from hovering, followed by deceleration toward the target, ending with a nonzero impact velocity, similar to what is observed in insects. Last, using an insect-scale flapping-wing aerial microrobot platform (Harvard RoboBee), we verified the controlled, safe, and accurate landing on natural terrain.

INTRODUCTION

For flying insects, successful transitions between aerial and terrestrial environments are a necessary function of daily life. Because flight has high energetic costs, insects must restore these losses by efficiently transitioning from air to substrates where they can rest or feed (*1*, *2*). Landing behavior among insects is diverse, with some species displaying more controlled flight strategies such as hovering or grazing to gradually decelerate as they touch down on a surface (*3*–*6*). However, other insects use more aggressive maneuvers, such as accelerating or crash-landing onto substrates (*7*–*9*). An important theme within insect landing research is the role of compliant legs in touchdown. Although the importance varies depending on approach velocity (for example, during acceleration versus deceleration), insect legs are usually extended before surface contact to absorb impact and allow engagement of tarsal attachment devices such as claws or adhesive pads (*2*, *4*, *5*). For example, Smith *et al.* (*9*) examined the landings of mosquitoes (*Aedes aegypti*) and observed that deceleration only occurred when certain appendages touched the surface. The long forelegs and proboscis essentially acted as dampers, dispersing impact force, sometimes causing the mosquito to bounce before reengaging with the surface.

For insects, diverse landing strategies may be a result of tradeoffs between morphology, substrates, and ecology, but insights into these mechanisms provide engineers with inspiration for producing more robust and adaptable aerial robots. For example, the benefits of compliant landing gear have already been explored across a range of kilogram-scale rotary-wing aerial robots (*10*–*12*); however, their importance for insect-scale flapping-wing microaerial vehicles (FWMAVs) remains largely unexplored (*13*). For smaller aerial robots, effectively distributing impact forces through a more passive means would be highly beneficial because weight restrictions may place limitations on the complexity of any "leg-like" structures or landing gear (*2*, *14*). In addition, softer transitions from air to land would benefit insect-scale FWMAVs, given that many are powered by small, delicate actuators that are easily fractured by external forces such as piezoelectric and electromagnetic actuators (*15*–*17*). Whereas prior work has used alternative actuation methods for FWMAVs, for example, soft dielectric elastomer actuators have demonstrated robustness for various collision scenarios (*17*), the wings of insect-scaled FWMAVs are also particularly vulnerable to damage from crashes. We therefore sought lightweight compliant legs that promote safe landings by absorbing impact energy and, thus, protect more delicate parts of the vehicle.

To test the role of passive joints and overall leg compliance, we built on an existing insect-scale FWMAV platform, the split actuator variant of the Harvard RoboBee (*18*). The RoboBee is a 100-mg FWMAV with a 30-mm wingspan that is powered by piezoelectric bimorph actuators that drive a high-frequency flapping-wing motion to generate thrust (at a flapping frequency of ~170 Hz). Using a geometric controller, sufficient control authority has been demonstrated to overcome previous limitations for yaw control authority of the RoboBee with only two wings (*19*). However, despite increased control authority, the task of landing is still difficult because of the generation, shedding, and subsequent interaction with vortices that also interact with nearby surfaces when hovering at low altitudes, known as the ground effect. The ground effect exacerbates the vehicle's already unstable dynamics and makes it difficult for the vehicle to safely and accurately land at a target position on a surface. This is further exacerbated by nonplanar, compliant, and dynamic surfaces, as we would expect in natural settings (*14*, *20*). To achieve safe and accurate landing with the RoboBee, we took inspiration from a group of large, flying insects known as crane flies (order Diptera). Crane flies have a body morphology similar to that of their close relatives, the mosquitoes; however, their body size is often of a scale (wingspan, body length) similar to that of the RoboBee family

---

[1] John A. Paulson School of Engineering and Applied Sciences, Harvard University, Massachusetts Hall, Cambridge, MA 02138, USA. [2] Elmore Family School of Electrical and Computer Engineering, Purdue University, 610 Purdue Mall, West Lafayette, IN 47907, USA.
†These authors contributed equally to this work.
*Corresponding author. Email: rjwood@seas.harvard.edu

(*21*, *22*). Similar to mosquitoes, crane flies have long legs relative to their body size that may serve as dampers to dissipate energy during landing impacts (*9*, *23*). Furthermore, crane flies have relatively weak flight capabilities, which results in frequent landings on a variety of surfaces (*23*, *24*). The crane fly's potential leg damping properties and their ability to land on a variety of surfaces are desirable features for FWMAVs and could provide a mechanical solution for robustly achieving safe and accurate landings. Previous leg designs for the RoboBee consisted of four rigid carbon fiber sticks of arbitrary length and placement for the sole purpose of standing the vehicle upright.

In this work, we took a more methodical approach to designing landing gear for FWMAVs by taking inspiration from different leg features as observed on crane flies. The leg features that were explored as a part of our design study included leg length and stance, viscoelastic materials for compliant leg joints, number of leg joints, and leg joint placement. We sought to understand which design parameters maximize energy dissipation during landings to improve landing safety. As a secondary motivation, we also aimed to minimize horizontal drift in position during landings to improve landing accuracy. Last, to complement the resulting inspired leg design, we introduced an updated adaptive controller and demonstrated safe and accurate landing, overcoming perturbations from the ground effect and irregularities of natural terrain.

RESULTS

Ground effect in controlled hovering flights

Conventionally, in larger, human-scale vehicles, the ground effect, an enhanced lift force when flying near a surface, was well studied for fixed-wing aircraft with forward translational motion and for hovering rotary-wing aircraft (*25*–*27*). As the vehicle moves away from the ground, a notable reduction in the ground effect is also observed for hovering rotary-wing vehicles at a height of approximately the diameter of the rotary wing (*27*). Similarly, the existence of the ground effect for flapping-wing vehicles has been shown using both simulation and experimental studies. In two-dimensional (2D) simulation studies, the ground effect clearance altitude was found to be two or three chord lengths (*28*). A second study involving a hovering vehicle with a flexible tail found that the clearance altitude is less than two chord lengths (*29*). On the other hand, the fountain effect, defined as an upward flow acting on the lower part of the body, was found in a 3D simulation, showing that an altitude of two chord lengths produces substantial ground effect when compared with an altitude of 15 chord lengths [which was defined as out-of-ground effect (*30*)]. The fountain effect was experimentally verified in hovering conditions near the ground by flapping the wing on a fixed stand with individually actuated wing stroke and pitch degrees of freedom (*31*, *32*). In these prior works, the border between in-ground effect and out-of-ground effect regions was not identified; these studies, instead, focused on the magnitude of the ground effect near the surface.

In the prior ground effect studies discussed above, the wing pitch (rotation) and wing stroke motions were directly controlled to follow sinusoidal trajectories, whereas wing rotation in the RoboBee is not directly actuated (*15*, *17*, *33*). Instead, the wing dynamics rely on passive rotation, and the rotational dynamics are a nonlinear function of wing velocity [with wing velocity being the parameter directly controlled (*34*); see movie S7 for a video showing passive wing rotation of the RoboBee].

The Harvard RoboBee offers an exemplary physical model to experimentally study the ground effect at the insect scale. The recent achievement of full attitude control for the RoboBee enables enhanced precision during hovering (*19*) while maintaining the heading angle, which is known to be the most challenging axis to control in the FWMAV literature (*35*). However, the controller was designed with the assumption that the FWMAV operates without any disturbances (no ground effect) or model parameter uncertainties. Thus, similar performance is not guaranteed while the vehicle is subject to the ground effect. Therefore, an adaptive controller was developed, extending our previous controller with the ability to compensate for model uncertainties and constant external disturbances. For example, a set of controlled hovering flight experiments using both nonadaptive control from (*19*) and the updated proposed adaptive controller was performed at a height of four wingspan lengths (avoiding the ground effect). A comparison of the performance of adaptive versus nonadaptive control is shown in Fig. 1C, which demonstrates improved lateral control accuracy by compensating for model uncertainties (see movie S6 for a video showing the improved lateral accuracy when using adaptive control). Depending on the target altitude, our result shows that the adaptive controller commands different thrust values, which offers an opportunity to quantify the ground effect. Details of the adaptive tracking controller design are described in the "Adaptive tracking controller design" section of the Supplementary Materials.

To quantify the ground effect, we first defined a metric that is a function of the dimensionless normalized height ratio (H) with respect to the wingspan of the vehicle. Let the height ratio be defined by

$$H = \frac{h_{\mathrm{cop}}}{l_{\mathrm{wing}}} \tag{1}$$

where h_{cop} is the distance between the landing platform to the median point of the wing roots (Fig. 2D), an approximation of the average center of pressure (COP) location between the two wings, and l_{wing} is the wingspan of the vehicle, measured to be 30 mm. The dimensionless height ratio is commonly used to define when the vehicle is in- or out-of-ground effect. Prior 3D computational studies of the ground effect for flapping-wing flight predict that an in-ground effect, with an 8% enhanced cycle-averaged lift force, occurs at $H = \sim 0.8$, relative to the case when H is 5.2, denoted as out-of-ground effect (*30*).

In this study, the difference between commanded thrust over varying height ratios H (Fig. 1, A and B) was used to identify the intensity of the ground effect as a function of H. We define the ground effect ratio, G, by

$$G = \left(1 - \frac{T_{\mathrm{avg}}}{T_{\mathrm{max}}}\right) \times 100\% \tag{2}$$

where T_{avg} is the commanded average thrust force of the vehicle at the hovering altitude and T_{max} is the maximum commanded thrust force of the vehicle taken over all hover experiments with various height ratios including around $H = 2.7$ (see Fig. 1A for the hovering height), which are interpreted as out-of-ground effect region in (*32*).

A total of 27 controlled hovering experiments were performed over the range $H \in (0.5, 3)$, as shown in Fig. 1A and movie S1. In our experimental controlled flight study, a gradual change in the ground

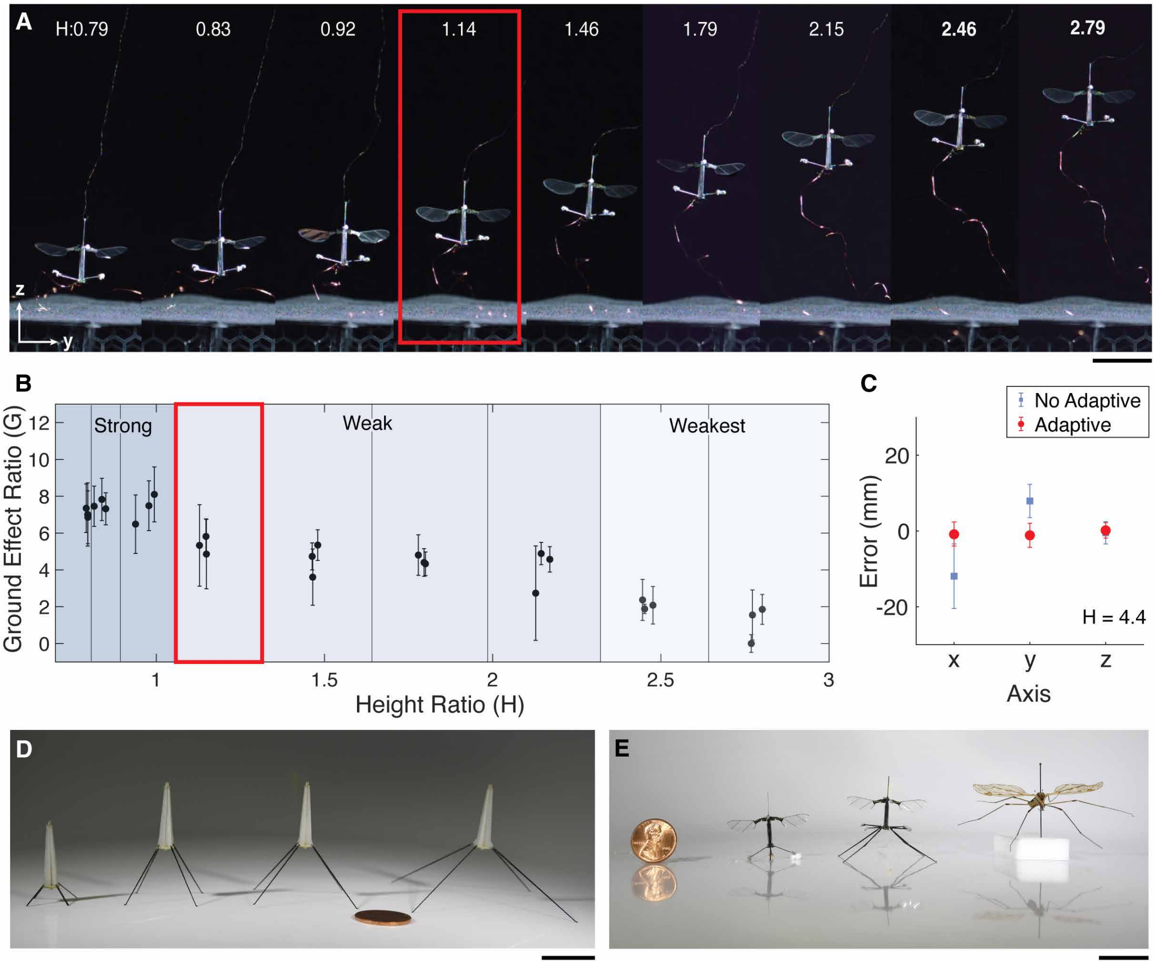

Fig. 1. Study of the ground effect. (**A**) Hovering flight experiments at different altitudes for studying the ground effect. The height-to-wingspan ratio is shown at the top. (**B**) Plot of the ground effect ratio (Eq. 2) as a function of the height-to-wingspan ratio (Eq. 1). The intensity of the ground effect is divided into three regions: strong (above 7%), weak (above 4%), and weakest (below 4%). The average and SD of the ground effect ratio within 2 s of hovering experiments (sample size $N = 20{,}000$) are shown with the dark circle and error bar, respectively. [(A) and (B)] The red boxes represent our desired leg height. (**C**) The hovering performance of two controllers, one without using the adaptive component from (*19*) and the other using the proposed adaptive controller hovering at $H = 4.4$ (weakest ground effect). The averaged lateral position error and its SD from 10 independent hovering experiments (sample size $N = 400{,}000$, 40-s flight) are shown with the dark circle and with the error bar, respectively. (**D**) Different leg stance designs installed on crash test dummy vehicles used for drop test experiments. The leg designs shown from right to left: legacy leg, narrow stance 30° leg, intermediate stance 45° leg, and wide stance 60° leg. All leg designs were rigidly attached to the dummy vehicles. (**E**) RoboBees with the legacy leg and compliant leg designs next to a US penny and a crane fly for scale. Scale bars, 20 mm [(A), (D), and (E)].

effect is shown in Fig. 1B, as opposed to a strict division of two regions as in (*30*). A noticeable change was observed near the height-to-wingspan ratio $H = 1.1$ (a 2% decrease in the ground effect ratio compared with the strong ground effect region) and $H = 2.3$ (a 2.4% decrease in the ground effect ratio compared with the weak ground effect region). Therefore, three ground effect regions based on the intensity of the ground effect ratio are proposed: The strong ground effect region is where G is greater than 7%, the weak ground effect region encompasses the ground effect ratio greater than 4% and less than 7%, and the weakest ground effect region is where the ground effect ratio is less than 4%. The mean and SD within these regions can be found in the fifth column of table S7. In addition, the tether (which provides power and control to the RoboBee) can inject forces that can potentially contribute to the augmented lift force measured during the hovering experiments. We performed a set of isolated tether stiffness experiments to quantify the differential force from $H = 1.14$ (the red-boxed altitude in Fig. 1A) to the lowest point in our experiments and found the peak force to be 4.9 μN, which is ~0.49% of the body weight (and, thus, also the ground effect ratio; analysis of the effect of the tether can be found in the Supplementary Materials). This is small relative to the ground effect ratios of 7.3 and 5.3% in the strong and the red-boxed regions in Fig. 1A, respectively. Thus, we consider the tether to apply random perturbations during our experiments.

The lowest altitude in the weak ground effect region, indicated by the red-boxed experiment in Fig. 1B, corresponds with a height $h_{cop} = 30$ mm. A simple mechanical solution to minimize perturbations from the ground effect is to design legs that elevate h_{cop} to be in the weak ground effect region when in contact with the ground. Therefore, we designed legs that lift the vehicle to $h_{cop} = 30$ mm, which equates to a leg height of $h_{leg} = 20$ mm. Figure 1D shows the extended leg design with three different stance angles installed on

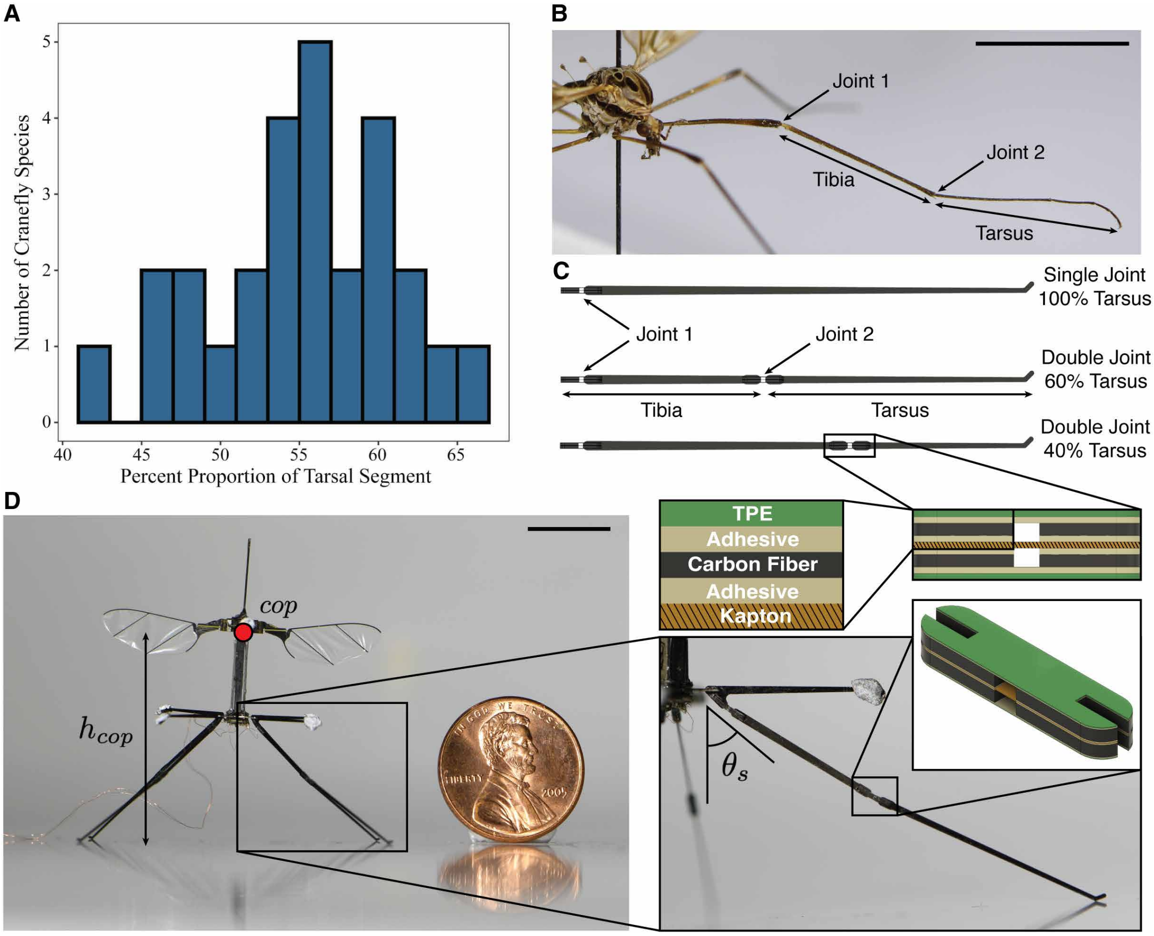

Fig. 2. Insect-inspired leg design. (**A**) Histogram of tarsal leg segment measurements of 27 different crane fly species. The horizontal axis represents the percentage of the leg that the tarsal segment occupies for a leg measurement consisting of tibia and tarsus segments shown in (B) and (C). The vertical axis represents the number of crane fly species that have a tarsal segment of a given leg percentage portion. (**B**) Close-up image of a giant crane fly (*Tipula abdominalis*) leg. The leg is labeled by the features of interest for the mechanical leg design shown in (C). (**C**) Illustration of different leg designs used in our landing studies. The one-joint leg represents a leg with no tibia. The two-joint legs were modeled off of a crane fly leg with both tibia and tarsus as labeled in (B). Two-joint legs with 60 and 40% proportion of tarsal segments were studied. The inset shows a blown-up image of the joint design used for the mechanical legs. The joint materials are labeled and color coded in the legend. (**D**) Image of the RoboBee with the two-joint compliant leg design installed. The close-up image of the leg shows the location of the mechanical joint as illustrated in (C). The average COP location is the red dot labeled "cop." The distance between the landing platform and the average COP is h_{cop}. The stance angle of the legs is θ_s. The compliant leg installed on the RoboBee is the two-joint variant with a 60% proportion tarsal segment. Scale bars, 10 mm [(B) and (D)]. Museum accession number for the crane fly specimen [seen in (B)] is MCZ-ENT-00806455.

nonfunctional dummy vehicles next to a dummy vehicle with the legacy leg design. By setting the leg design to a height where the vehicle operates outside the strong ground effect region, we minimized vehicle instability when landing.

Insect-inspired leg design and fabrication

The proposed stance height in the previous section ensures that the FWMAV remains within the weak ground effect region when the robot lands vertically. However, upon contact with the ground, a destabilizing moment can affect controller performance. Although the accuracy of hovering control near the surface was improved using the proposed adaptive controller, the SD of the center of mass (CoM) position to the targeted hovering point stays around 3 mm (Fig. 1C). Therefore, for FWMAVs operating in close proximity to a surface, ground impacts are unavoidable (see movie S8 for an example of a failed landing using rigid legs). Furthermore, destabilizing forces acting on the leg during a crash can cause the wings (one of the most vulnerable components) to violently collide with the ground. This can damage the wing and transmit impact forces to the actuator. At worst, when the wing is actively flapping during a collision, the forces transmitted to the actuator can approximately double the actuator blocked force, resulting in a high probability of actuator and/or wing failure (*34*).

For larger aircraft, pneumatic tires attached to shock-absorbing struts are used to dissipate energy during landing (*36*). This energy absorber–style landing gear is highly effective at dissipating energy and is ideal for larger passenger aircraft where large impulses must be avoided for vehicle safety and passenger comfort. For smaller aircraft with stricter weight limitations, the heavy shock-absorbing landing gear is typically replaced with rigid struts (such as in the "taildragger" landing gear configuration) that rely on material deformation in the strut and energy absorption in pneumatic tires to dissipate energy upon landing (*37*). Likewise, microaerial vehicles and robots have an extremely limited payload capacity [a maximum of 100 mg for the RoboBee (*18*)], making the weight of a landing gear a major consideration in vehicle design. For this reason, simpler mechanisms composed of compliant beams are more appropriate for subgram aerial robots such as the RoboBee. Our proposed leg design for subgram aerial robots was, in part, inspired by the minimal beam/truss structures in the landing gears of lightweight human-piloted aircraft.

The first criterion to ensure safe landing is to understand the support polygon created by the tips of the legs. We chose four legs for our design to strike a balance between sufficient contact support areas while minimizing added weight from additional legs. A detailed analysis of the leg contact support area is outlined in the Supplementary Materials. The second criterion to enhance postcollision stability involves how much kinetic energy is dissipated during the landing impact phase. The jointed legs of insects (Fig. 2B) may help dissipate kinetic energy (*9*). Therefore, we added compliant joints that deform in response to impacts, thereby reducing the moments imparted on the robot's CoM. To determine the number and location of the joints, we looked to the crane fly for inspiration. Focusing on the tibia and tarsus, these segments of the crane fly leg are largely separated by two major joints as shown in Fig. 2B, where joint 1 connects the tibia and joint 2 connects the tarsus. The relative segment lengths were chosen on the basis of measurements taken from museum specimens of 27 crane fly species [from Harvard MCZbase (*38*)], which are shown in the histogram in Fig. 2A. Most crane fly species measured had a longer tarsal proportion between 55 and 60%. Therefore, we investigated various tarsal proportions as a design parameter in Fig. 2C. The percent proportion of the tarsus varied between 100, 60, and 40%. Among these choices, we analyzed the kinetic energy dissipation after the impact using the coefficient of restitution (CoR) as discussed below.

The joints that separate the tarsus and tibia were constructed using a combination of thin film materials to act as a rotational spring and damper system. We took inspiration from a previous design of damping joints (*39*) that served as collapsible buckling hinges for the wing of an FWMAV to replicate the damping behavior of the costal break of a wasp wing. The synthetic costal break buckling hinge in (*39*) successfully dampened wing collisions with surfaces to mitigate damage from impacts. A similar lossy behavior is desired for our synthetic leg to dissipate energy from collisions during vehicle landings. The joints were constructed using bulk micromachining and lamination methods (*40*), consisting of a flexible polyimide (Dupont Kapton) film sandwiched between two layers of carbon fiber composite sheets. Two layers of viscoelastic thermoplastic elastomer (TPE; Airtech Stretchlon 200) were laminated on the outside to sandwich the Kapton and carbon fiber joint. The Kapton acts as a spring element for the joint, and the TPE acts as a damping element. The joint stiffness properties were altered using different thicknesses of the Kapton layer. The thickness of the Kapton was tuned such that it could support the weight of the vehicle while standing. The damping joints are shown in Fig. 2D installed on the RoboBee with a 60% tarsus, double joint leg design. The joint laminate layup is shown in the inset in Fig. 2D, with the layer colors corresponding to the material used. To characterize the stiffness and damping properties of the Kapton-TPE joints, we performed a series of unforced oscillation experiments to estimate lumped-parameter spring and damping constants (see the "Compliant joint characterization" section in the Supplementary Materials and movie S2 for the experimental setup).

Analysis of leg designs for safe and accurate landing

The unforced oscillation experiments allowed us to quantitatively explore the design space of the joint, including geometric and material parameters, with the hypothesis that greater energy absorption at the joint will lead to improved landing. We connected this hypothesis to our landing experiments by proposing three quantitative metrics for safe and accurate landing: CoR, lateral drift (Δx), and landing success (e). Evaluating these metrics for various landing scenarios and leg designs enabled us to choose the leg stance angles and compliant damping joint properties to achieve reliable landing.

The first metric is the CoR, which quantifies energy dissipation during landing collision. The second metric is the Δx of the vehicle from immediately before to immediately after a landing collision, which quantifies the accuracy of the vehicle landing. The third metric is the success rate for landing (e) in the upright position after surface collision.

The CoR is defined by

$$\mathrm{CoR} = \left|\frac{v_2}{v_1}\right| \tag{3}$$

where v_1 is the vehicle velocity just before surface impact and v_2 is the vehicle velocity just after surface impact (Fig. 3, A and B). The purpose of the CoR analysis is to compare the energy dissipation of each leg design; the lower the CoR is, the closer the landing approximates an inelastic collision, which, in turn, results in a safer and more accurate landing.

The horizontal drift metric is defined by

$$\Delta x = |x_{\mathrm{final}} - x_{\mathrm{initial}}| \tag{4}$$

where x_{initial} is the vehicle's horizontal position at the moment the vehicle is dropped and x_{final} is the vehicle's final horizontal position after landing. The purpose of the horizontal drift analysis is to compare the error between the final landing position and the desired target landing position during the drop test.

A series of six free-fall tests was performed for 12 different leg designs to determine the best combination of joint materials and tarsus length ratio. The CoR and Δx measurements are tabulated in table S5 and plotted in Fig. 3 (D and E). The leg designs labeled with numbers 1 to 12 are listed in table S4. Note that we have excluded the joint design with TPE only (no Kapton) and the joint design with TPE and 7.5-μm Kapton (table S3) from our free-fall experiments for leg designs with joint 1 and no joint 2. We excluded these joints from our parameter set because, when installed on the vehicle in a one–joint leg design, the legs buckle at the joints and the base of the vehicle collides with the ground. If the legs cannot support the vehicle's weight, this is not a viable design as a safe landing platform.

For the design process, we followed an incremental procedure where we first studied the stance angle (θ_s in Fig. 2D) for rigid legs (legs 2 to 4). We then compared the stiffness of the compliant joints (legs 5 and 6). Last, we compared the tarsus length ratios (legs 5 to 12) to find the optimal design with respect to the two performance indexes, CoR and Δx. We found that the minimal CoR design does not result in the minimum horizontal drift error. However, the differences between the horizontal drift errors among adjacent designs remain relatively minimal compared with the achieved reduction in

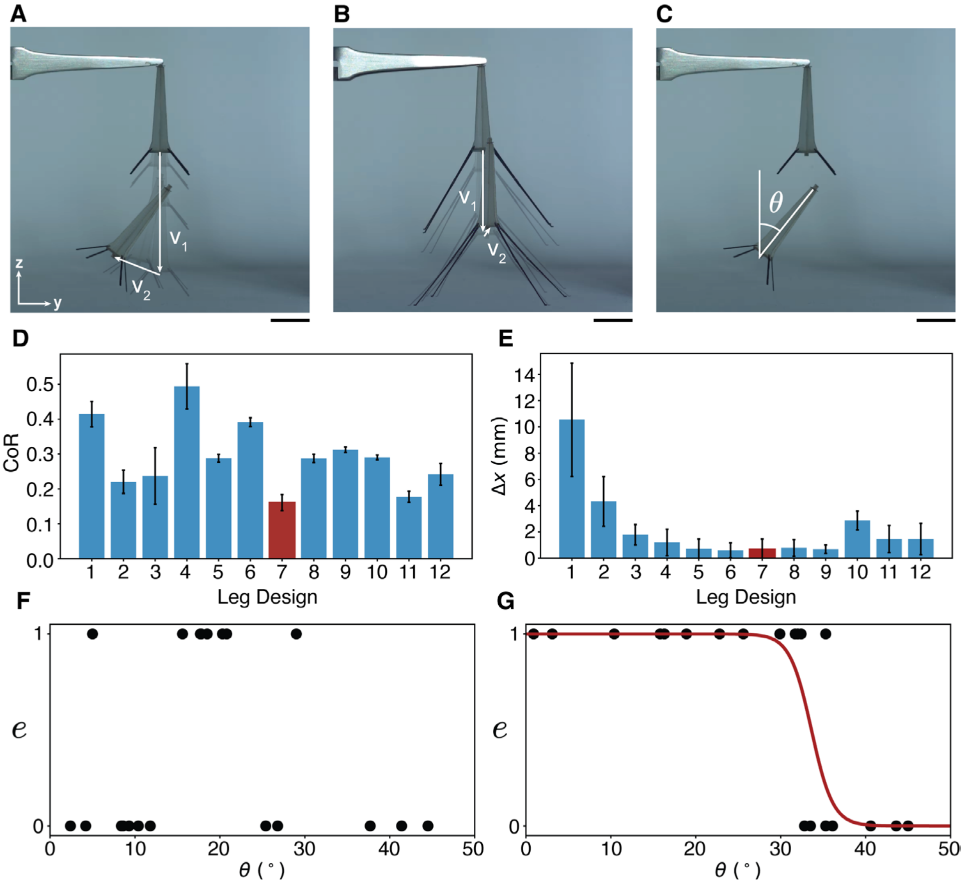

Fig. 3. Free-fall experiments. (**A**) Sequence from a free-fall experiment for a crash-test dummy vehicle with the legacy leg design (leg 1) installed (see movie S3). Vectors v_1 and v_2 depict the vehicle velocity before and after ground collision. (**B**) Sequence from a drop-test experiment for a crash-test dummy vehicle with the compliant leg design (leg 7) installed. (**C**) Image from a drop-test experiment in (A) depicting the body angle θ measurement. Scale bars, 10 mm. (**D**) Comparison of the CoR metric and (**E**) Δx metric between all leg designs tested. The average and SD of the CoR and Δx experiments (sample size $N = 5$) are shown by the bar height and error bar, respectively. The red bars in (D) and (E) show the chosen leg design used in the subsequent controlled flight-landing experiments and demonstration. (**F**) Plot of the landing success metric for the crash test dummy vehicle with the legacy leg design installed. The landing success metric, $e \in \{0, 1\}$, is characterized by whether the vehicle lands upright after ground collision ($e = 1$ represents landing success). (**G**) Plot of e for a crash-test dummy vehicle with the compliant leg design (leg 7) installed, corresponding with the experiment depicted in (B). These are fitted using a classification logistic regression model to illustrate the predictability of landing success over different body angles.

CoR. The chosen leg design is highlighted in red in Fig. 3 (D and E) (see the "Experimental approach to leg design" section in the Supplementary Materials for details on leg design choice based on the CoR and Δx metrics).

The two metrics (CoR and Δx) focus on the behavior immediately after impact, assuming an upright attitude of the vehicle during free fall. The third metric is the success rate of landing upright to analyze the range of body roll orientations that ensure an upright landing for the chosen compliant leg design (leg 7). The e metric is denoted as 1 if the vehicle landed upright and 0 otherwise (Fig. 3, F and G). A series of 20 drop tests was performed while varying the vehicle body roll angle at drop between the range θ∈(0°, 50°), where θ is the body roll angle with respect to the vertical axis (Fig. 3C). The drop tests were performed for the legacy leg (leg 1) and the chosen compliant leg (leg 7) designs, and the results are plotted in Fig. 3F. For the legacy leg, we note that landing success is not directly correlated with the body roll angle θ during free fall. This is due to the high CoR for the legacy design, which increases the angular kinetic energy after collision, causing the vehicle to tumble.

In contrast with the legacy leg design (leg 1), landing success for the compliant leg design (leg 7) provides consistent successful upright landing at modest body roll angles (Fig. 3G). We used a binary classification model to generate a prediction for whether the vehicle will succeed in landing upright based on the body roll angle θ when the vehicle approaches the surface. The range of body angles that result in successful upright landings for the compliant leg design (relative to the unpredictable success of the legacy leg design) highlights a substantial increase in the passive upright landing success rate. On the basis of this landing success classification model, our controller commands the vehicle's body angle to be |θ| < 30° relative to a horizontal landing substrate to ensure a high probability of landing successfully (see the "Experimental approach to leg design" section in the Supplementary Materials for details on the landing success classification model).

Although the leg design analysis was only conducted with the robot constrained to straight vertical landing, the same methodology can be adapted for other, more difficult landing conditions. For example, for a landing condition where the vehicle velocity has a horizontal component, experiments can be conducted where the robot is commanded to fly with various forward velocities and body attitudes (θ) before landing. By sweeping a range of initial velocities and body angles at ground contact, a map of landing success can be obtained as a function of both leg properties and control parameters. Furthermore, previous studies have been conducted on landing under difficult conditions, such as perching on a vertical surface using an iterative learning–based controller (*41*). Our safe landing methodology could be merged with such a controller to further improve the robot's probability of landing success.

Similarly, our leg design can be further generalized for landing on surfaces with different orientations. To achieve this, an adhesion mechanism would be required to allow the vehicle to stick to the surface. Both magnetic and electrostatic adhesion mechanisms have been used to perch the RoboBee on vertical and inverted surfaces (*41*, *42*). These adhesion mechanisms could be attached to the feet of our compliant leg design to enable the robot to land on surfaces with different orientations while retaining the benefit of dissipating energy during landing.

Flight and landing control

Controlled landing is one of the most challenging tasks for unpiloted aerial vehicles because of the difficulty in adapting to sudden changes in airflow (such as when subject to the ground effect) and impulsive impacts experienced upon touching the surface. Landing success depends strongly on controlled deceleration as the body gets close to the target. Many flying insects, including fruit flies and bumblebees, have limited perception for distance estimation and do not directly measure the distance to the target but, instead, use optic flow to gauge the rate of relative retinal expansion to safely decelerate as they approach the target (*43*–*45*). This rate of expansion is inversely proportional to a metric called the time-to-contact, τ, which is defined as

$$\tau(t) = -\frac{z(t)}{\dot{z}(t)}, \gamma(t) = \frac{1}{\tau(t)} \tag{5}$$

where $z(t)$ is the vertical distance to the target in the inertial frame, $\dot{z}$ is the approach velocity to the target surface, and γ is the convergence rate that captures the rate of retinal expansion velocity as described in (*45*). Setting a constant τ ratio ($\dot{\tau} = 0$) ensures a safe landing, which is observed in honey bee (*44*), fruit fly (*Drosophila melanogaster*) (*45*), and bumblebee landing (*46*). Furthermore, ~35.7% of landings of fruit flies are crash landings (for example, wing or head collision with nonzero impact velocity), whereas most failures are due to late leg extension (*45*). The proposed compliant leg design in this paper provides an opportunity to study safe crash landing (with nonzero impact velocity) because the legs are already deployed.

The τ theory alone does not specify the low-level control algorithms needed for safe landing (how to modify the flapping patterns to maintain the exact τ profile). Instead, τ theory has inspired engineers to generate trajectories for many applications, including unpiloted aerial vehicle landing on the deck of a ship (*47*) and the design of a safe landing trajectory for a lunar lander using the lunar images (*48*). In contrast with these landing studies that neglect the ground effect and are based on larger-scale rotorcraft, the role of closed-loop control in the presence of the ground effect to track τ theory trajectories using insect-scale FWMAVs still remains a challenge.

In previous biological landing studies, τ theory was well suited to describe the landing behavior when initiated from a nonzero initial velocity (when a specimen is already moving toward the target). The use of τ theory was not envisioned for trajectories initiated from rest, which requires the vehicle to accelerate initially. More recently, researchers have observed that bumblebees use optical cues to both decelerate and accelerate while approaching a landing target (*49*). In these studies, they use a simple model with a constant γ derivative ($\dot{\gamma}$) to define the acceleration at the beginning phase of landing (still with nonzero velocity). However, there exists a phase in the experiments where a constant $\dot{\gamma}$ does not imply acceleration when the velocity is too high, which suggests the need for a more general theory to capture acceleration using the τ values.

To account for more general acceleration profiles, we consider the role of the second derivative of γ, which offers a decision criterion for designing the acceleration and deceleration phases, a requirement for transitions between different hovering points (see the "Landing trajectory design" section in the Supplementary Materials). In subsequent landing experiments, the RoboBee was commanded to land on a target starting from hovering. Therefore, we propose a trajectory such that the sign of the second derivative of γ indicates the initial acceleration and deceleration before landing. Inspired by observations of fruit fly landing sequences in (*45*), we proposed the following landing sequence: First, command the vehicle to hover above the target at the upper boundary of the weak ground effect region (Fig. 1B). Next, command the vehicle to follow the τ theory–inspired trajectory to initially accelerate and then decelerate toward the ground effect boundary. Last, when the vehicle is near the lower boundary of the weak ground effect region (the red-boxed region in Fig. 1B), turn off power and allow the vehicle to absorb residual kinetic energy.

The guiding trajectory offering the smooth transition from the initial hovering height $h_i \in \mathbb{R}$ to the desired landing height $h_f \in \mathbb{R}$ is defined as

$$z(t) = h_d \frac{(1 - \tanh \alpha t)}{2} \tag{6}$$

where $z(t)$ is the vertical distance from the initial height to the landing height, $h_d = h_i - h_f$. The α parameter controls the rate of acceleration and deceleration of the landing trajectory. The second derivative of the convergence rate model ($\ddot{\gamma}$) for this guiding trajectory can be calculated as

$$\ddot{\gamma} = -\frac{2\alpha}{h_d}\ddot{z} \tag{7}$$

which is proportional to the acceleration $\ddot{z}$. The sign of $\ddot{\gamma}$ indicates that the vehicle will accelerate for the first half of the landing sequence in $(h_d/2, h_d)$ and decelerate for the last half of the sequence in $(0, h_d/2)$. Therefore, we designed the landing trajectory for the RoboBee on the basis of $\ddot{\gamma}$ as a function of $z(t)$. $\ddot{\gamma}$ provides a framework to design generalized landing behavior for FWMAVs (see the "Adaptive tracking controller design" section in the Supplementary Materials for the detailed derivation).

After the proposed landing sequence and the landing trajectory in Eq. 6, we performed a series of controlled flight tests on the RoboBee with four different α values. For controlled flight experiments, the robot is controlled via an off-board target computer to follow *X*, *Y*, and *Z* trajectories (the dashed line targets in fig. S8). Real-time state estimation is achieved via external infrared motion capture cameras (Vicon T-Series) to track retroreflective markers placed on the vehicle. The power and control signals are connected through a copper wire tether to actuate the wings of the robot. The experimental setup used to perform the controlled flight tests is illustrated in fig. S7.

First, our controlled flight experiments consist of vertical takeoff and landing on a smooth rigid surface as shown in Fig. 4A and movie S4. In these experiments, we specify the target landing height to be either below ground (10 mm lower for $\alpha = 3$) or exactly at the target surface ($\alpha = 5$, 7, and 9). From the initial hovering altitude near the upper boundary of the weak ground effect region ($H = 2.0$), the RoboBee accelerates and tracks the positive second derivative of $\ddot{\gamma}$ as shown in Fig. 4E. The velocity profile during the landing sequence for four experiments is shown in Fig. 4F. During the acceleration period (the dark blue region in Fig. 4F), the RoboBee descends with a maximum velocity ranging from 0.5 ms^{-1} ($\alpha = 3$) to 1.8 ms^{-1} ($\alpha = 9$) proportional to the α values. Next, the RoboBee decelerates (medium blue region in Fig. 4F) before the power turns off (light blue region in Fig. 4F). The aggressiveness of the landing can be modified by choice of α, where the maximum descending velocity varies from 0.04 to 0.17 ms^{-1} to achieve maximum deceleration

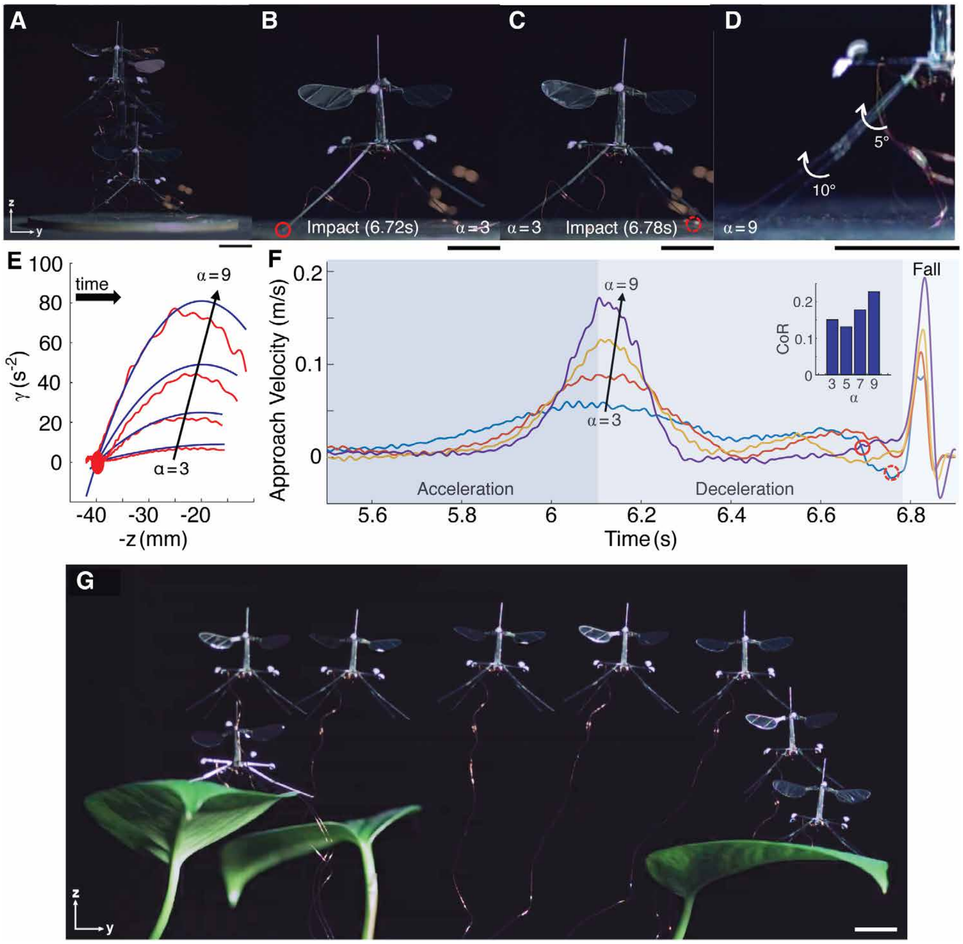

Fig. 4. Controlled flight evaluations and demonstrations. (**A**) Example sequence from takeoff and landing experiments performed to characterize trajectory tracking accuracy. (**B** and **C**) Snapshot of a landing ($\alpha = 3$) making multiple leg contacts. The red circle indicates the contact point. (**D**) An example ($\alpha = 9$) from a collision, using overlaid images before and after leg contact, showing bending of the two leg joints. (**E**) Plot of the first derivative of the convergence rate model $\dot{\gamma}$ as a function of vehicle altitude, z, for different acceleration rates, $\alpha \in [3, 5, 7, 9]$. The experimental trajectories are plotted in red, and $\dot{\gamma}$ for different values of α is plotted in blue. (**F**) The approach velocity for different values of α (positive values indicate a faster approach). The dark blue and medium blue regions represent acceleration and deceleration toward the ground, respectively. The plots in the light blue region represent free fall. The solid and dashed red circles indicate the contact moments shown in (B) and (C), respectively. The CoR of four landing experiments is also shown with the bar graph inset. (**G**) Demonstration of controlled takeoff and landing of the RoboBee with lossy compliant legs (leg 7) from the left leaf to the right leaf. Scale bars, 10 mm (all panels).

values from 0.2 to 2.0 ms^{-2} in this study. However, the proposed landing gear has increased mass and inertia (18 mg, 19% of the total weight increase, and increased yaw moment of inertia by 531%; see table S6). The adaptive controller builds on our recent improvements to yaw control using multiple harmonic signals (*19*) rather than the more typical "split-cycle" method (*18*). Using the adaptive controller, we show that the heading angle can be controlled even with augmented mass and inertia (see movie S4).

In the first experiment (the least aggressive landing case, $\alpha = 3$), the target position of the tip of the leg was commanded to be 10 mm below the ground. As the robot descends toward the ground, the compliant leg touches the ground multiple times (two images capturing the impact are shown in Fig. 4A). The impact velocity of the vehicle was 0.08 ms^{-1}, which is relatively slow because the robot was tracking the least aggressive trajectory. Previously, an impact during landing with the rigid legacy leg would lead to an unpredictable landing, causing the vehicle to tumble and potentially damage the wings (see movie S8 for an example landing failure). In this experiment ($\alpha = 3$), the vehicle decelerated further while experiencing multiple leg tip collisions with the ground (two red circles in Fig. 4, B and C), which demonstrates the ability of our lossy compliant legs to further dissipate the kinetic energy of the vehicle during landing.

The energy dissipation through our proposed leg design was further verified in the other three tests, where the CoR among vertical landing experiments remained similar to what we tested using dummy vehicles (Fig. 4F). In particular, the most aggressive landing ($\alpha = 9$) showed that the adaptive controller was able to accelerate as desired but took an early deceleration when compared with its reference trajectory (Fig. 4E). This results in the vehicle behaving as an underdamped system, oscillating around an offset above ground (fig. S8). Thus, in this experiment, the vehicle entered the free-fall phase at a higher altitude, causing it to impact the ground with the highest velocity among the four experiments (1.9 ms^{-1}). As a result, the compliant leg joint was bent to a maximum angle of 5° between the base of the vehicle and the tibia leg segment and 10° between the tibia and tarsal leg segments (see movie S4, landing experiment $\alpha = 9$). Because the coefficient of the restitution for our proposed leg design was small, the vehicle maintained contact with the ground without bouncing.

With the demonstration of consecutive takeoff and landing using our compliant leg design and bioinspired landing sequence, we demonstrated the success of our mechanical and control designs on a natural terrain environment. We performed a takeoff and landing task with the RoboBee from one leaf of a pothos plant to another leaf as illustrated in Fig. 4G. The vehicle was commanded to first take off from the starting leaf, hover, move laterally to the second leaf, and hover 5 cm above the leaf ($H = 2.6$; in the weakest ground effect region shown in Fig. 1B). Next, the vehicle followed the τ landing sequence to descend to 0.7 cm above the leaf ($H = 1.2$), which is in the lower bound of the weak ground effect region, and lastly free fell to land on the second leaf while dissipating any remaining energy in the legs. The same experimental setup for the previous controlled flight tests was used for the leaf-to-leaf landing demonstration, the only difference being the introduction of a plant branch in the motion capture arena. The target trajectories for commanding the robot to fly from one leaf to the other leaf are represented by dashed lines in fig. S8. The target takeoff and landing locations on the leaves were measured before the experiment by placing retroreflective markers on the leaf surfaces and gathering their X, Y, and Z positions via the motion capture cameras.

For the leaf-landing task, we used $\alpha = 3$ as the rate of acceleration and deceleration in the landing sequence. We found that even on a compliant landing substrate, the vehicle could safely land on an incline, where the compliant legs conform to the concave leaf surface. In movie S5, the vehicle lands at a different body orientation from the hovering and landing orientation because of the inclined surface of the leaf. This is analogous to the landing success metric analysis (Fig. 3, C, F, and G) because after hovering at the lower weak ground effect region, the vehicle falls freely to the target. The landing orientation of the vehicle at impact (because of the incline of the leaf surface) is 6°, which is within the fitted landing success classifier function and shown in Fig. 3G (see the "Experimental approach to leg design" section in the Supplementary Materials for details on the classification model).

During landing, the two right legs contact the surface first because of a slight positive roll just before landing. However, the contact moment between the leaf and the right legs is insufficient to make the vehicle tip over, whereas the additional flat "foot" on the end of the tarsus helps the legs to slide (see inset of Fig. 2D). Therefore, the vehicle stabilizes successfully in the upright position. In addition, the initial contact with the compliant right legs dissipates the vehicle's kinetic energy upon surface contact, which reduces the kinetic energy associated with subsequent leg impacts. Last, the leaf slightly oscillates after the initial contact, but the vehicle successfully lands upright (movie S5).

CONCLUSIONS

The low mass and small scale of FWMAVs lend themselves to landing on and exploring delicate surfaces in natural terrain without damaging their environments. Our compliant leg design provides a simple mechanical solution for FWMAVs to achieve the difficult task of robust landing on natural terrain, opening possibilities to future applications such as environmental monitoring, surveillance, or manipulation of delicate organisms. Not only do compliant legs enable FWMAVs to robustly land on a variety of surfaces, but their energy dissipation properties also help to preserve the vehicle's lifespan. The primary drawbacks of piezoelectric actuators for microrobots are their fragility and low fracture toughness. Compliant legs aid in protecting the delicate piezoelectric actuators from collision-induced fractures during crash landings by increasing the envelope of landing success through deliberate leg stance and leg joint–damping material selection. With more mechanically robust vehicles, we can increase the development rate of FWMAVs to more quickly achieve the aforementioned applications. Furthermore, our leg design serves as a platform for the future possibility of leg joint actuation. This could be made possible by small-scale soft actuators such as dielectric elastomer actuators, which are manufactured using a laminate manufacturing process similar to that of our damping joint design and are constructed of compliant viscoelastic materials that can be tuned to the desired damping properties of our current damping joint design. Actuated joints would open possibilities for multimodal locomotion or manipulation, self-righting capabilities in case of landing failure, and active control of legs during flight to control the oscillatory behavior of the legs as was observed during flight experiments conducted in this work.

Robots for biology

In addition to facilitating safe landings for FWMAVs, our RoboBee platform highlights an intriguing tool for exploring biological questions. Although adaptations from biological organisms can provide engineers with insight into effective bioinspired designs, biologists can also use engineering-based methods to produce appropriate physical models for biomechanics research (*50–53*). Insect legs are quite diverse in form and function, and our current study serves as just an initial exploration of leg joint materials and segment length. For example, insect tarsi are usually subdivided into multiple segments with additional joints, producing a highly flexible limb that facilitates tasks such as terrestrial locomotion, feeding, and landing. The distribution and size of these tarsomeres are quite variable among different groups, and future work could explore how the concentration of additional joints facilitates landing during different touchdown maneuvers and across diverse terrains. In addition to landing studies, the modularity of the RoboBee's components (detachable legs, wings, airframe, and actuators) produces an adaptable platform useful for comparative studies exploring other parameters of interest (such as wing design and landing surface attachment devices) relevant to insect flight.

Limitations and future work

Although the proposed mechanical and algorithmic approaches enhance landing success for an insect-scale flapping-wing vehicle, there are several additional challenges to ensure robust landing on diverse substrates. First, the role of lossy compliant joints when landing on uneven (inclined) surfaces remains an open question. We believe that one promising route could involve active control during leg-to-substrate collisions to further compensate for disturbances from interactions with rough or uneven terrain. Second, landing robustness for higher impact velocities, as observed in the landing strategies of stingless bees (*8*) and mosquitoes (*9*), can be studied to further tune the mechanical damping of the multisegment joints. Third, the scalability of the proposed approaches to larger vehicles should be investigated. As a vehicle increases in size, the absolute payload also generally increases, which may offer opportunities to explore more complex leg geometries and the integration of actuated joints and active or passive adhesion mechanisms. Scaling metrics can be used to guide such studies, for example, the landing mechanism mass fraction and the overall vehicle damping ratio. Last, at larger scales, full landing autonomy can be assisted by integrating an onboard sensor package [for example, including biomimetic ocelli (*54*) or neuromorphic sensors (*55*)] for lower latency state feedback.

In summary, we presented a bioinspired integrated framework to overcome some of the landing challenges for insect-scale flapping-wing aerial vehicles. This framework offers insights into how to maximize energy dissipation during landing collisions while actively controlling the system. We believe that the foundation of passive energy dissipation with multijoint segments and active control during landing can be applied more broadly to investigate contact-rich tasks for flapping-wing aerial vehicles operating in proximity to environmental objects.

MATERIALS AND METHODS

Unforced oscillation experiment for leg joint characterization

Unforced oscillation experiments were performed to characterize the legs and leg joints. The experiments were performed by manually perturbing the leg by an initial distance of $F_{d,0}$ (defined in eq. S2) and then releasing the leg to observe the resulting oscillations, as shown in fig. S1B. Each of the experiments was captured using high-speed video (Phantom v710, Vision Research, captured at 3000 frames/s). The angular position of the leg during free oscillation was extrapolated using a physics tracking software (Physlets Tracker). From these unforced oscillation experiments, we observed that the system response of the leg and joint behaves as an underdamped spring-mass-damper model with viscoelastic creep. From these experimental observations, we modeled the leg and joint system as in eq. S6.

Free-fall landing experimental setup

A series of free-fall tests were performed for the leg designs listed in table S4 to quantify the three landing performance metrics for defining safe and accurate landing: CoR (table S5), Δx (table S5), and e (Fig. 3, F and G). Each of the leg designs was assembled on nonfunctional crash-test dummy vehicles constructed from woven fiberglass (FR-4), shown in Fig. 3 (A to C). The crash dummy vehicles were designed with a mass and inertia similar to those of the functional split-actuator RoboBee used in subsequent flight experiments. Each dummy vehicle was held at a fixed height (40 mm from ground to CoM) using reverse-action tweezers mounted to a fixed table clamp. The dummy vehicles were manually released such that they free fell to the ground. Each free-fall test was captured using high-speed video (Phantom v710, Vision Research, captured at 3000 frames/s). The position of the CoM of the dummy vehicles during free fall was determined using a physics tracking software (Physlets Tracker). The velocities of the dummy vehicles during free fall were determined using numerical differentiation.

Statistical analysis

The average and the SD for N sampled data, $\{x_i\}_{i=1}^{N} \subset \mathbb{R}$, shown in Fig. 1 (B and C) and Fig. 3 were calculated using the following equation:

$$\overline{x} := \frac{\sum_{i=1}^{N} x_i}{N}, \sigma := \sqrt{\frac{\sum_{i=1}^{N} \left(x_i - \overline{x}\right)^2}{K}} \quad (8)$$

where $\overline{x}$ is the average and σ is the SD with $K = N - 1$ for Fig. 1 (B and C), where $N \geq 20{,}000$, and with $K = N$ for Fig. 3, where the sample size is relatively small ($N = 5$).

Supplementary Materials

The PDF file includes:

Supplementary Text
Figs. S1 to S9
Tables S1 to S7
Legends for movies S1 to S8
References (*56*–*62*)

Other Supplementary Material for this manuscript includes the following:

Movies S1 to S8

REFERENCES AND NOTES

1. R. Dudley, *The Biomechanics of Insect Flight: Form, Function, Evolution* (Princeton Univ. Press, 2000).
2. W. Roderick, M. Cutkosky, D. Lentink, Touchdown to take-off: At the interface of flight and surface locomotion. *Interface Focus* **7**, 20160094 (2017).
3. M. Srinivasan, S. Zhang, J. Chahl, E. Barth, S. Venkatesh, How honeybees make grazing landings on flat surfaces. *Biol. Cybern.* **83**, 171–183 (2000).
4. C. Evangelista, P. Kraft, M. Dacke, J. Reinhard, M. Srinivasan, The moment before touchdown: Landing manoeuvres of the honeybee *Apis mellifera*. *J. Exp. Biol.* **213**, 262–270 (2010).
5. T. Reber, E. Baird, M. Dacke, The final moments of landing in bumblebees, *Bombus terrestris*. *J. Comp. Physiol. A Neuroethol. Sens. Neural. Behav. Physiol.* **202**, 277–285 (2016).
6. P. Goyal, E. Baird, M. Srinivasan, F. Muijres, Visual guidance of honeybees approaching a vertical landing surface. *J. Exp. Biol.* **226**, jeb245956 (2023).
7. P. Tichit, I. Alves-Dos-Santos, M. Dacke, E. Baird, Accelerated landing in a stingless bee and its unexpected benefits for traffic congestion. *Proc. R. Soc. B* **287**, 20192720 (2020).
8. K. Shackleton, N. J. Balfour, H. A. Toufailia, D. A. Alves, J. M. Bento, F. L. W. Ratnieks, Unique nest entrance structure of *Partamona helleri* stingless bees leads to remarkable 'crash-landing' behaviour. *Insectes Soc.* **66**, 471–477 (2019).
9. N. Smith, J. Balsalobre, M. Doshi, B. Willenberg, A. Dickerson, Landing mosquitoes bounce when engaging a substrate. *Sci. Rep.* **10**, 15744 (2020).
10. S. B. Baker, D. Soccol, A. Postula, M. Srinivasan, "Passive landing gear using coupled mechanical design" in *Proceedings of Australasian Conference on Robotics and Automation* (AARA, 2013), pp. 1–8.
11. K. Zhang, P. Chermprayong, D. Tzoumanikas, W. Li, M. Grimm, M. Smentoch, S. Leutenegger, M. Kovac, Bioinspired design of a landing system with soft shock absorbers for autonomous aerial robots. *J. Field Robot.* **36**, 230–251 (2019).
12. W. R. T. Roderick, M. R. Cutkosky, D. Lentink, Bird-inspired dynamic grasping and perching in arboreal environments. *Sci. Robot.* **6**, eabj7562 (2021).
13. A. Hammad, S. Armanini, Landing and take-off capabilities of bioinspired aerial vehicles: A review. *Bioinspir. Biomim.* **19**, 031001 (2024).
14. H. Liu, S. Ravi, D. Kolomenskiy, H. Tanaka, Biomechanics and biomimetics in insectinspired flight systems. *Philos. Trans. R. Soc. B* **371**, 20150390 (2016).
15. K. Ma, P. Chirarattananon, S. Fuller, R. Wood, Controlled flight of a biologically inspired, insect-scale robot. *Science* **340**, 603–607 (2013).
16. Y. Zou, W. Zhang, Z. Zhang, Liftoff of an electromagnetically driven insect-inspired flapping-wing robot. *IEEE Trans. Robot.* **32**, 1285–1289 (2016).
17. Y. Chen, H. Zhao, J. Mao, P. Chirarattananon, E. F. Helbling, N. P. Hyun, D. R. Clarke, R. J. Wood, Controlled flight of a microrobot powered by soft artificial muscles. *Nature* **575**, 324–329 (2019).
18. K. Y. Ma, S. M. Felton, R. J. Wood, "Design, fabrication, and modeling of the split actuator microrobotic bee" in *2012 IEEE/RSJ International Conference on Intelligent Robots and Systems* (IEEE, 2012), pp. 1133–1140.
19. R. McGill, N. P. Hyun, R. J. Wood, Modeling and control of flapping-wing micro-aerial vehicles with harmonic sinusoids. *IEEE Robot. Autom. Lett.* **7**, 746–753 (2021).
20. M. Matthews, S. Sponberg, Hawkmoth flight in the unsteady wakes of flowers. *J. Exp. Biol.* **221**, 179259 (2018).
21. A. R. Ennos, The kinematics and aerodynamics of the free flight of some Diptera. *J. Exp. Biol.* **142**, 49–85 (1989).
22. C. A. Triplehorn, N. F. Johnson, D. J. Borror, *Borror and DeLong's Introduction to the Study of Insects* (Thompson Brooks/Cole, ed. 7, 2004).
23. H.-M. Hu, G. Watson, B. Cribb, J. Watson, Non-wetting wings and legs of the cranefly aided by fine structures of the cuticle. *J. Exp. Biol.* **214**, 915–920 (2011).
24. C. P. Ellington, The aerodynamics of hovering insect flight. III. Kinematics. *Philos. Trans. R. Soc. Lond. B* **305**, 41–78 (1984).
25. J. Zerihan, X. Zhang, Aerodynamics of a single element wing in ground effect. *J. Aircr.* **37**, 1058–1064 (2000).
26. J. Molina, X. Zhang, Aerodynamics of a heaving airfoil in ground effect. *AIAA J.* **49**, 1168–1179 (2011).
27. C. Pasquali, J. Serafini, G. Bernardini, J. Milluzzo, M. Gennaretti, Numerical-experimental correlation of hovering rotor aerodynamics in ground effect. *Aerosp. Sci. Technol.* **106**, 106079 (2020).
28. T. Gao, X.-Y. Lu, Insect normal hovering flight in ground effect. *Phys. Fluids* **20**, 087101 (2008).
29. J. Wu, C. Liu, S.-C. Yang, N. Zhao, Influence of a flexible tail on the performance of a foil hovering near the ground: Numerical investigation. *Eur. J. Mech. B Fluids* **52**, 85–96 (2015).
30. M. Maeda, H. Liu, Ground effect in fruit fly hovering: A three-dimensional computational study. *J. Biomech. Sci. Eng.* **8**, 344–355 (2013).
31. T. Van Truong, J. Kim, M. J. Kim, H. C. Park, K. J. Yoon, D. Byun, Flow structures around a flapping wing considering ground effect. *Exp. Fluids* **54**, 1575 (2013).

32. H. Lu, K. B. Lua, Y. Lee, T. Lim, K. Yeo, Ground effect on the aerodynamics of three-dimensional hovering wings. *Bioinspir. Biomim.* **11**, 066003 (2016).
33. Y. M. Chukewad, J. James, A. Singh, S. Fuller, RoboFly: An insect-sized robot with simplified fabrication that is capable of flight, ground, and water surface locomotion. *IEEE Trans. Robot.* **37**, 2025–2040 (2021).
34. N. T. Jafferis, M. A. Graule, R. J. Wood, "Non-linear resonance modeling and system design improvements for underactuated flapping-wing vehicles" in *Proceedings of the International Conference on Robotics and Automation 2016* (IEEE, 2016), pp. 3234–3241.
35. Z. Tu, F. Fei, L. Liu, Y. Zhou, X. Deng, Flying with damaged wings: The effect on flight capacity and bio-inspired coping strategies of a flapping wing robot. *IEEE Robot. Autom. Lett.* **6**, 2114–2121 (2021).
36. R. K. Schmidt, *The Design of Aircraft Landing Gear* (SAE International, 2021).
37. N. S. Currey, *Aircraft Landing Gear Design: Principles and Practices* (American Institute of Aeronautics and Astronautics, 1988).
38. *MCZbase: The Database of the Zoological Collections* (Museum of Comparative Zoology, Harvard Univ., 2024).
39. A. M. Mountcastle, E. F. Helbling, R. J. Wood, An insect-inspired collapsible wing hinge dampens collision-induced body rotation rates in a microrobot. *J. R. Soc. Interface* **16**, 20180618 (2019).
40. J. P. Whitney, P. S. Sreetharan, K. Y. Ma, R. J. Wood, Pop-up book MEMS. *J. Micromech. Microeng.* **21**, 115021 (2011).
41. P. Chirarattananon, K. Y. Ma, R. J. Wood, Perching with a robotic insect using adaptive tracking control and iterative learning control. *Int. J. Robot. Res.* **35**, 1185–1206 (2016).
42. M. A. Graule, P. Chirarattananon, S. B. Fuller, N. T. Jafferis, K. Y. Ma, M. Spenko, R. Kornbluh, R. J. Wood, Perching and takeoff of a robotic insect on overhangs using switchable electrostatic adhesion. *Science* **352**, 978–982 (2016).
43. H. Wagner, Flow-field variables trigger landing in flies. *Nature* **297**, 147–148 (1982).
44. E. Baird, N. Boeddeker, M. R. Ibbotson, M. V. Srinivasan, A universal strategy for visually guided landing. *Proc. Natl. Acad. Sci. U.S.A.* **110**, 18686–18691 (2013).
45. F. van Breugel, M. H. Dickinson, The visual control of landing and obstacle avoidance in the fruit fly *Drosophila melanogaster*. *J. Exp. Biol.* **215**, 1783–1798 (2012).
46. J. J. Chang, J. D. Crall, S. A. Combes, Wind alters landing dynamics in bumblebees. *J. Exp. Biol.* **219**, 2819–2822 (2016).
47. H. Lin, B. Wang, C. Tang, G. Xu, "Autonomous landing of a VTOL UAV on a ship based on tau theory" in *Proceedings of the 34th Chinese Control and Decision Conference* (IEEE, 2022), pp. 2785–2790.
48. G. De Croon, D. Izzo, G. Schiavone, Time-to-contact estimation in landing scenarios using feature scales. *Acta Futura* **5**, 73–82 (2012).
49. P. Goyal, J. L. van Leeuwen, F. T. Muijres, Bumblebees land rapidly by intermittently accelerating and decelerating toward the surface during visually guided landings. *iScience* **25**, 104265 (2022).
50. N. Gravish, G. Lauder, Robotics-inspired biology. *J. Exp. Biol.* **221**, jeb138438 (2018).
51. G. Lauder, Robotics as a comparative method in ecology and evolutionary biology. *Integr. Comp. Biol.* **62**, 721–734 (2022).
52. W. Barley, L. Ruge-Jones, A. Wissa, A. Suarez, M. Alleyne, Addressing diverse motivations to enable bioinspired design. *Integr. Comp. Biol.* **62**, 1192–1201 (2022).
53. A. Wissa, M. Alleyne, W. C. Barley, A. V. Suarez, Best practices of bioinspired design: Key themes and challenges. *Integr. Comp. Biol.* **62**, 1147–1152 (2022).
54. S. B. Fuller, M. Karpelson, A. Censi, K. Y. Ma, R. J. Wood, Controlling free flight of a robotic fly using an onboard vision sensor inspired by insect ocelli. *J. R. Soc. Interface* **11**, 20140281 (2014).
55. S. Stroobants, J. Dupeyroux, G. C. de Croon, Neuromorphic computing for attitude estimation onboard quadrotors. *Neuromorph. Comput. Eng.* **2**, 034005 (2022).
56. B. M. Finio, N. O. Pérez-Arancibia, R. J. Wood, "System identification and linear time-invariant modeling of an insect-sized flapping-wing micro air vehicle" in *Proceedings of the International Conference on Intelligent Robots and Systems 2011* (IEEE, 2011), pp. 1107–1114.
57. M. H. Dickinson, F.-O. Lehmann, S. P. Sane, Wing rotation and the aerodynamic basis of insect flight. *Science* **284**, 1954–1960 (1999).
58. J. Zhang, Z. Tu, F. Fei, X. Deng, "Geometric flight control of a hovering robotic hummingbird" in *Proceedings of the International Conference on Robotics and Automation 2017* (IEEE, 2017), pp. 5415–5421.
59. F. A. Goodarzi, D. Lee, T. Lee, Geometric adaptive tracking control of a quadrotor unmanned aerial vehicle on SE (3) for agile maneuvers. *J. Dyn. Syst. Meas. Control* **137**, 091007 (2015).
60. K. S. Narendra, A. M. Annaswamy, *Stable Adaptive Systems* (Courier Corporation, 2012).
61. J. W. Grizzle, C. Chevallereau, R. W. Sinnet, A. D. Ames, Models, feedback control, and open problems of 3D bipedal robotic walking. *Automatica* **50**, 1955–1988 (2014).
62. P. Ramdya, R. Thandiackal, R. Cherney, T. Asselborn, R. Benton, A. J. Ijspeert, D. Floreano, Climbing favours the tripod gait over alternative faster insect gaits. *Nat. Commun.* **8**, 14494 (2017).

Acknowledgments
Funding: This material is based on work supported by the National Science Foundation Graduate Research Fellowship Program under grant no. DGE 2140743. Any opinions, findings, and conclusions or recommendations expressed in this material are those of the author(s) and do not necessarily reflect the views of the National Science Foundation. **Author contributions:** N.P.H. and R.J.W. proposed and designed the research. All authors wrote and provided feedback on the paper. N.P.H. designed the controller and tautheory-based trajectories and conducted the ground effect experiments and analysis. C.M.C. and A.M.H. designed the bioinspired legs. C.M.C. fabricated the legs and performed leg design optimization with experiments. C.M.C. conducted the controlled vertical landing experiments and leaf-to-leaf demonstrations. N.P.H. analyzed the controlled flight experiments. **Competing interests:** The authors declare that they have no competing interests. **Data and materials availability:** All (other) data needed to evaluate the conclusions in the paper are present in the paper or the Supplementary Materials. The controlled flight data and the leg design experiments can be found at DOI 10.5061/dryad.n02v6wx7r.

Submitted 7 May 2024
Accepted 18 March 2025
Published 16 April 2025
10.1126/scirobotics.adq3059

Science Robotics

Sticking the landing: Insect-inspired strategies for safely landing flapping-wing aerial microrobots

Nak-seung P. Hyun, Christian M. Chan, Alyssa M. Hernandez, and Robert J. Wood

Sci. Robot. **10** (101), eadq3059. DOI: 10.1126/scirobotics.adq3059

Science Robotics (ISSN 2470-9476) is published by the American Association for the Advancement of Science. 1200 New York Avenue NW, Washington, DC 20005. The title *Science Robotics* is a registered trademark of AAAS.